Fuel Processing Technology 158 (2017) 226–237

Contents lists available at ScienceDirect

Fuel Processing Technology

journal homepage: www.elsevier.com/locate/fuproc

Research article

Comprehensive CFD modelling of solar fast pyrolysis of beech wood pellets

José Soria [a], Kuo Zeng [b,1], Daniela Asensio [a], Daniel Gauthier [b], Gilles Flamant [b,*], Germán Mazza [a]

[a] Institute for Research and Development in Process Engineering, Biotechnology and Alternative Energies (PROBIEN, CONICET - UNCo), 1400 Buenos Aires St., 8300 Neuquén, Argentina
[b] Processes, Materials and Solar Energy Laboratory (PROMES-CNRS, UPR 8521), 7 Rue du Four Solaire, Odeillo, 66120, Font-Romeu, France

ARTICLE INFO

Article history:
Received 23 November 2016
Received in revised form 3 January 2017
Accepted 7 January 2017
Available online 24 January 2017

Keywords:
CFD
Solar pyrolysis
Beech wood
High temperature
High heating rate
Single particle model

ABSTRACT

The present work focuses on the study of the solar pyrolysis of beech wood pellets. The biomass degradation process was modelled in the CFD (Computational Fluid Dynamics) platform ANSYS FLUENT 14.0. The results of simulations were compared to experimental tests conducted in a lab-scale solar reactor in order to validate the CFD model. The biomass pyrolysis was carried out at temperatures ranging from 600 to 2000 °C, at two heating rates: 10 and 50 °C/s. This new 2D single particle model represents a significant improvement of previous simpler version, not only because it allows monitoring the evolution of gas speciation but also because its formulation enables to deal with different types of biomass feedstock. The model structure comprises a multi-step complex kinetic framework that involves competitive reactions –including secondary tar reaction- along with rigorous heat and mass (species) transport inside the particle.

On this basis, char, tar and gas predicted yields are compared with experimental data. In addition, the gas composition (CH_4, CO, CO_2, H_2 and C_xH_y) is also compared. CFD results are in good agreement with the experimental values, validating this approach as a useful tool to predict the products yields and their composition when pyrolyzing biomass particles. Furthermore, the model can be used when modelling any process where pyrolysis occurs and it can even be easily coupled to any reactor scale model.

1. Introduction

In the last two decades and as a result of the growing energy demand and of the concern of greenhouse gases emissions from fossil fuel combustion, there has been an increasing interest in renewable and environmentally friendly energy sources. Biomass energy technology stands as a promising option among others [1–3]. Among the different biomass conversion methods, thermochemical treatment is often employed; and pyrolysis is considered as one of the most attractive pathways to transform biomass into condensable gas (tar and water), permanent gas (H_2, CO, CO_2, CH_4, C_2H_6) and char, that can be subsequently upgraded to fuels [4–7]. Moreover, the yields and product distribution depend on the operating conditions and feedstock properties [8–10].

Nonetheless, pyrolysis is globally endothermic and it requires heat, which is classically provided by any fossil fuel combustion in conventional processes. This drawback can be overcome by using concentrated solar radiation as the energy source of the process, which increases the energy conversion efficiency and reduces the pollution discharge [11]. In a direct heating solar reactor, fast/flash pyrolysis (high levels of temperatures and heating rates -HR-) can be achieved since the biomass directly absorbs concentrated solar radiation, tending to yield more gas products, particularly high quality syngas [12]. Solar reactors represent an interesting alternative, when compared to conventional reactors, due to its flexibility to operate for a wide range of temperature (600–2000 °C) and heating rate (5–450 °C/s) while minimizing the energy cost [13]. Therefore, direct solar pyrolysis allows to produce more combustible gas with a higher heating value than the one obtained in traditional reaction units [14], which can be then used as fuel for power generation, heat or transportable fuel production.

The transient formation of char and release of gas and tar are governed by the pyrolysis rate. In the case of a large particle – such as the pellet dealt with in this work –, the magnitude of this rate is determined either by the heat transfer in the pellet or by both the heat transfer and kinetic rates [15]. This "thermally thick" condition leads to non-uniform biomass temperatures during pyrolysis. Additionally, the intra-particle residence time in large biomass particle may be sufficient for tar decomposition reactions to occur inside the particle. Moreover, at high heating rates, the produced char layer can act as a catalyst. As a result, the intra-particle tar cracking reactions modify the product yields by reducing the amount of produced emitted tar, and they increase the amount of light gaseous products escaping the particle. Also, this secondary tar decomposition may take place in the vapor phase (homogeneous) and on the surface of the pyrolyzing solid (heterogeneous). Even more, secondary tar cracking can also happen inside (intra-particle) or outside (extra-particle) the biomass particle [16,17].

* Corresponding author.
E-mail address: gilles.flamant@promes.cnrs.fr (G. Flamant).
[1] Present address: *State Key Laboratory of Coal Combustion, Huazhong University of Science and Technology, Wuhan 430074, China.*

http://dx.doi.org/10.1016/j.fuproc.2017.01.006
0378-3820/

Nomenclature

A	Pre-exponential factor, s^{-1}
C_P	Specific heat capacity, J/kg.K
d	Diameter, m
D	Diffusivity, m^2/s
e	Particle emissivity
E_a	Activation energy, J/kmol
k	Thermal conductivity, W/(m.K)
K	Permeability, m^2
M	Molecular weight, kg/kmol
P	Pressure, Pa
r	Reaction rate, kg/(m^3.s)
r	Radial coordinate, m
R	Radius, m
R	Gas law constant, 8314 J/(kmol.K)
S	Source term, kg/(m^3.s)
S_v	Specific surface area, m^2/m^3
t	Time, s
T	Temperature, K
u	Gas velocity, m/s
x	Axial coordinate, m
x_B	Biomass conversion, dimensionless
Y	species mass fraction, dimensionless

Greek letters

α	Stoichiometric coefficient
β	Heating rate, °C/s
Δh	Reaction enthalpy, J/kg
ε	Porosity
τ	Particle tortuosity
ρ	Apparent density, kg/m^3
$\hat{\rho}$	Intrinsic density, kg/m^3
σ	Stephan-Boltzmann constant, 5.67 10^{-8} W/m^2K^4
μ	Viscosity, Pa.s

Subscripts

0	Initial
B	Biomass
C	Char
eff	Effective
g	Gas
H Init	Enthalpy initial
s	Solid
sec	Secondary

Abbreviations and chemical formulas

2D-DP	Two Dimensional Double Precision solver
AR	Argon
CELL	Cellulose
CELLA	Activated cellulose
CFD	Computational Fluid Dynamics
CO	Carbon monoxide
CO_2	Carbon dioxide
CH_2O	Formaldehyde
CH_3OH	Methanol
CH_3CHO	Acetaldehyde
CH_4	Methane
C_2H_4	Ethylene
C_2H_5OH	Ethanol
C_3H_6O	Propanal
FE2MACR	Sinapaldehyde
G{CO_2}	Trapped CO2
G{CO}	Trapped CO
G{CH_2O}	Trapped CH2O
G{CH_4}	Trapped CH4
G{C_2H_4}	Trapped C2H4
G{CH_3OH}	Trapped CH3OH
G{H_2}	Trapped H2
GLYOX	Glyoxal
H_2	Hydrogen
HAA	Hydroxyacetaldehyde
HCE	Hemicellulose
HCEA1	Activated hemicellulose 1
HCEA2	Activated hemicellulose 2
HCOOH	Formic acid
HMFU	5-hydroximethyl-furfural
HR	Heating Rate
H_2O	Water vapor
LIG	Lignin
LIG-C	Carbon-rich lignin
LIG-H	Hydrogen-rich lignin
LIG-O	Oxigen-rich lignin
LIG-CC	Carbon-rich lignin 2
LIG-OH	OH-rich lignin
LVG	Levoglucosan
PHENOL	Phenol
pCOUMARYL	Paracoumaryl alcohol
UDF	User Defined Function
XYLAN	Xylose monomer

Modelling thermochemical processes at the pellet scale (local scale) can be a very useful tool for achieving a deep understanding of the interaction between chemical and physical phenomena during solid consumption, and of the influence of variables such as temperature, heating rate, particle size and biomass composition [18]. Particularly, accurate pyrolysis modelling represents a very complex and challenging task [19], not only because there are still some uncertainties regarding transcendental aspects of pyrolysis, but also because the physical and chemical phenomena as well as the aforementioned parameters have an important impact on the pyrolysis behaviour [20].

In this sense, several numerical approaches have been developed in order to study the kinetics of the thermal decomposition of biomass [21–28]. However, most previous models were developed based on experimental results at low heating rates and low temperature. Okekunle et al. [29] and Zeng et al. [30] formulated numerical models to represent biomass pyrolysis at moderate and high temperatures and heating rates, but their models were narrowed to three lumped products (tar, gas and char) and limited to only one type of biomass: Japanese cypress and beech, respectively.

In this context, the aim of this work is to develop a CFD single particle model based on competitive, multi-component kinetic mechanisms [31] -taking into account homogeneous intra-particle secondary tar reaction-, capable of predicting tar and gas species compositions when pyrolyzing "thermally thick" biomass particles. The model is validated against experimental data obtained in a lab-scale solar reactor assisted by a 1.5 kW solar furnace, for final temperatures of 600, 900, 1200, 1600 and 2000 °C and two values of heating rate (HR): 10 and 50 °C/s.

2. Experimental method

2.1. Material

The beech sawdust particles were dried in an oven to remove their total moisture content, and then compressed into cylindrical pellets with 10 mm in diameter and 5 mm thick. The beech pellet composition and its properties are given in Tables 1 and 2, respectively. In Table 1,

Table 1
Beech wood composition.

Ultimate analysis (wt.%, d.b)					Proximate analysis (wt.% d.b)			Biochemical analysis (wt.%, d.b)				
C	H	O	N	S	Volatile matter	Fixed C	Ash	CELL	HCE	LIGC	LIGH	LIGO
50.8	5.9	42.9	0.3	0.02	85.3	14.3	0.4	46	32	8.33	9.61	4.06

Table 2
Beech pellet properties.

Property	ε_0	L_0 [m]	R_0[m]	$\rho_{B,0}$ [kg/m^3]
Value	0.365	5.10^{-3}	5.10^{-3}	764

CELL stands for cellulose, HCE for hemicellulose, LIGO for oxygen-rich lignin, LIGC for carbon-rich lignin and LIGH for hydrogen-rich lignin.

2.2. Solar reactor experimental set-up

Fig. 1 depicts the setup applied for carrying out the solar pyrolysis experiments. The reactor consists of a transparent Pyrex® spherical balloon, with argon used as the working flow medium in order to take out the volatiles products. The pellet was placed in a graphite crucible insulated with graphite foam and placed at the focus of a 1.5 kW vertical-axis solar furnace. Also the pellet remained static during whole experiment. The sample surface temperature was measured by a solar-blind optical pyrometer. The heating rate and the final temperature are controlled by a PID controller that mastered the incident radiation by means of a shutter. A vacuum pump was used to take out the pyrolysis gas along with argon. A detailed description regarding the experimental procedure can be found in ref. [13].

3. CFD single particle model

The modelling configuration and the boundary conditions are presented in Fig. 2. Fig. 2a displays the sun-irradiated biomass pellet in the transparent reactor. The biomass pellet is treated as a porous medium with cylindrical shape of radius R_0 and height L_0, insulated by the crucible and foam at the lateral and bottom walls. Due to symmetry, half of the pellet is considered as the computational domain (2D axi-symmetric case), as shown in Fig. 2b. Extra-particle tar secondary reactions are excluded from the analysis.

The adopted reaction mechanism combines the detailed pyrolysis scheme developed by Ranzi et al. [31] –recently, Corbetta et al. (2014) [15] presented an update of this scheme, but it has not been employed in this work- and a proposed homogeneous secondary tar reaction scheme, which is supposed to be relevant for particles of a certain thickness. Additionally, these reaction mechanisms ensure a high flexibility to deal with different types of feedstock.

The source terms in the transport equations (mass, momentum, chemical species and energy) are implemented in the pyrolysis model by means of User-Defined Functions (UDFs) in C++ language. Moreover, additional UDFs were included in order to take into account the solid mass conservation, porosity and permeability changes as the reaction proceeds, as well as effective thermal conductivities and diffusion coefficients.

3.1. Main assumptions

The two-dimensional axis-symmetric pyrolysis model is based on the following assumptions:

1. The biomass pellet is cylindrical and homogeneous.
2. Structural changes, such as shrinkage, swelling, and cracks formation during pyrolysis are not considered.
3. Inside the pellet, the solid and gas phases are assumed to be in local thermal equilibrium, with identical internal temperatures and their gradients.
4. Gas phase follows ideal gas law.
5. The pellet structure is isotropic.

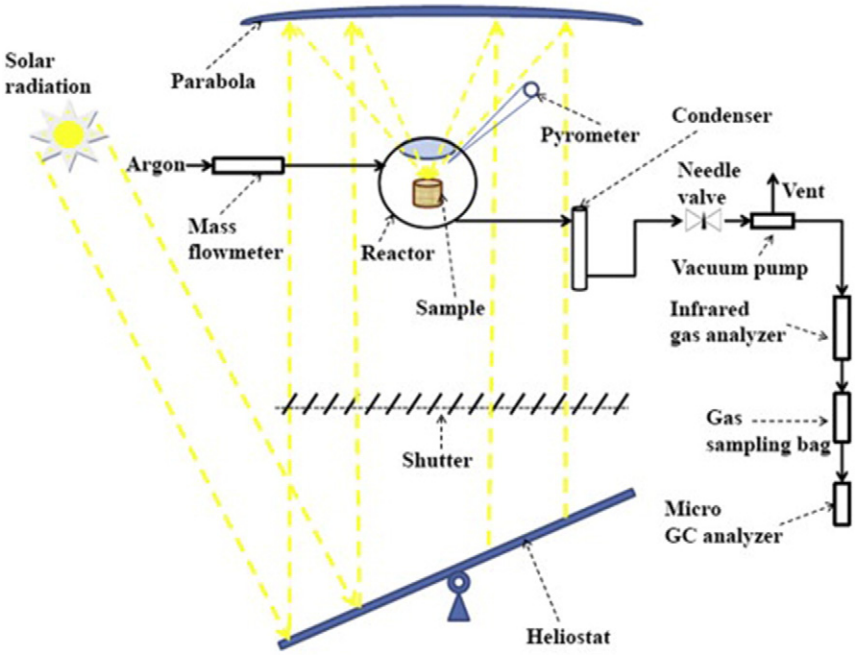

Fig. 1. Schematic of the solar pyrolysis experimental set-up [13].

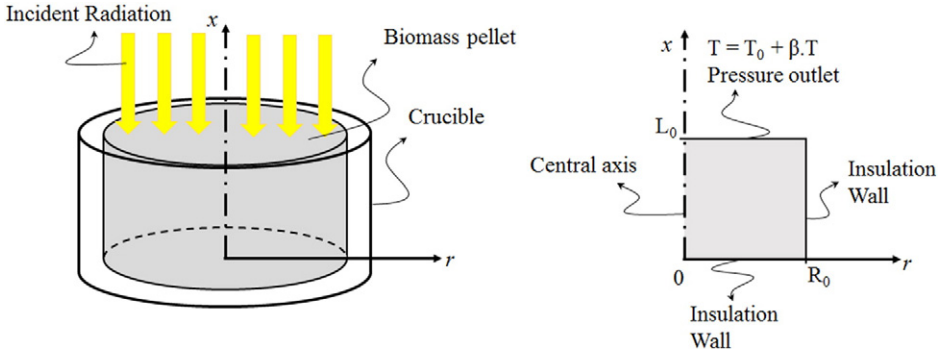

Fig. 2. Schematic of the computational domain and boundary conditions.

6. The heat transport due to species diffusion is negligible.
7. A volumetric heat source is used to consider the thermal decomposition. A constant value of heat of pyrolysis is assumed.
8. Radiative transfer equation is not modelled. Instead, the radiant contribution is comprised in a radiant conductivity.
9. Gasification reactions due to the H_2O and CO_2 released during pyrolysis are not considered.
10. Tar secondary heterogeneous reaction is not considered.

3.2. Governing equations

The governing equations: energy, continuity, species (for gaseous and tar species), momentum and solid species mass are presented hereafter.

Species mass transport equation

$$\frac{\partial\left(\varepsilon\rho_g Y_i\right)}{\partial t}+\frac{\partial\left(\rho_g u_x Y_i\right)}{\partial x}+\frac{\partial\left(r\rho_g u_r Y_i\right)}{r\partial r} = \frac{\partial}{\partial x}\left(D_{eff,g}\frac{\partial\left(\rho_g Y_i\right)}{\partial x}\right)+\frac{\partial}{r\partial r}\left(rD_{eff,g}\frac{\partial\left(\rho_g Y_i\right)}{\partial x}\right)+S_{g,i}. \quad (1)$$

Overall gas-phase continuity equation

$$\frac{\partial\left(\varepsilon\rho_g\right)}{\partial t}+\frac{\partial\left(\rho_g u_x\right)}{\partial x}+\frac{\partial\left(r\rho_g u_r\right)}{r\partial r}=S_g. \quad (2)$$

x-Momentum equation

$$\frac{\partial\left(\varepsilon\rho_g u_x\right)}{\partial t}+\frac{\partial\left(\rho_g u_x u_x\right)}{\partial x}+\frac{\partial\left(r\rho_g u_r u_x\right)}{r\partial r} = -\frac{\partial p}{\partial x}-\frac{\mu}{K}u_x+2\frac{\partial}{\partial x}\left(\mu\frac{\partial u_x}{\partial x}\right)+\frac{\partial}{r\partial r}\left(r\mu\left(\frac{\partial u_x}{\partial r}+\frac{\partial u_r}{\partial x}\right)\right). \quad (3)$$

Table 3
Main thermo-physical values adopted in the model.

Property	Value	Reference
ε_0 [−]	0.365	Measured
L_0 [m]	$5\cdot10^{-3}$	Measured
r_0 [m]	$5\cdot10^{-3}$	Measured
C_{pB} [J/(kg·K)]	2300–1150.exp.(−0.0055 × T)	[32]
C_{pC} [J/(kg·K)]	1430 + 0.355 × T − 7.32.10^7 × T^{-2}	[32]
$d_{pore,C}$ [m]	$4\cdot10^{-4}$	[39]
$d_{pore,B}$ [m]	$4\cdot10^{-5}$	[39]
$\rho_{B,0}$ [kg/m^3]	764	Measured
$\hat{\rho}_C$ [kg/m^3]	2000	[32]
K_B [m^2]	$1\cdot10^{-12}$	[32]
K_C [m^2]	$1\cdot10^{-11}$	[32]
e [−]	0.95	Measured
k_B [W/(m·K)]	0.291 + 0.000836 × 0.33 × T	[26]
k_C [W/(m·K)]	1.47 + 0.0011 × T	[40]

r-Momentum equation

$$\frac{\partial\left(\varepsilon\rho_g u_r\right)}{\partial t}+\frac{\partial\left(\rho_g u_x u_r\right)}{\partial x}+\frac{\partial\left(r\rho_g u_r u_r\right)}{r\partial r} = -\frac{\partial p}{\partial r}-\frac{\mu}{K}u_r+2\frac{\partial}{r\partial r}\left(r\mu\frac{\partial u_r}{\partial r}\right)+\frac{\partial}{\partial x}\left(\mu\left(\frac{\partial u_x}{\partial r}+\frac{\partial u_r}{\partial x}\right)\right)-2\mu\frac{u_r}{r^2}. \quad (4)$$

Energy conservation equation

$$\frac{\partial\left(\left(\rho C_p\right)_{pm}T\right)}{\partial t}+\frac{\partial\left(\rho_g C_{pg}u_x T\right)}{\partial x}+\frac{\partial\left(r\rho_g C_{pg}u_r T\right)}{r\partial r} = \frac{\partial}{\partial x}\left(k_{eff}\frac{\partial T}{\partial x}\right)+\frac{\partial}{r\partial r}\left(rk_{eff}\frac{\partial T}{\partial r}\right)+S_h. \quad (5)$$

With $(\rho C_p)_{pm}=\sum_s \rho_{s,i}C_{ps,i}+\sum_g \varepsilon\rho_{g,i}C_{pg,i}$.

Solid mass conservation equation

$$\frac{\partial\rho_{s,i}}{\partial t}=S_{s,i}. \quad (6)$$

The mass and energy source terms are given by
For the solid phase:

$$S_i=-\sum_{r,i=react}A_r\exp\left(-\frac{E_a}{RT}\right)\rho_i + \sum_{r,i\neq react}\alpha_i\frac{M_i}{M_{reac}}A_r\exp\left(-\frac{E_a}{RT}\right)\rho_{react}\Big|_{Sec.\ \ Reac}. \quad (7)$$

For tars:

$$S_i=-\sum_{r,i=react}A_r\exp\left(-\frac{E_a}{RT}\right)\varepsilon\rho_i\Big|_{Sec.\ \ Reac} + \sum_{r,i\neq react}\alpha_i\frac{M_i}{M_{reac}}A_r\exp\left(-\frac{E_a}{RT}\right)\rho_{react}. \quad (8)$$

For permanent gas

$$S_i=\sum_{r,i\neq react}\alpha_i\frac{M_i}{M_{reac}}A_r\,exp\left(-\frac{E_a}{RT}\right)\rho_{react} + \sum_{r,i\neq react}\alpha_i\frac{M_i}{M_{reac}}A_r\,exp\left(-\frac{E_a}{RT}\right)\varepsilon\rho_{react}\Big|_{Sec.\ \ Reac} \quad (9)$$

$$S_h=-\sum_r\Delta h_i S_i-\sum_{s,g}S_i\int_{T_{ref}}^{T}C_{p,i}dT. \quad (10)$$

3.3. Boundary conditions

The boundary conditions for the above equations are:

(1) For the top surface under radiation ($x = L_0$),

$$T = T_{exp}(t) = T_0 + \beta t; \quad Y_i = 0;\ Y_{Ar} = 1;\ P = P_0 \tag{11}$$

where β is the heating rate.

(2) For the sidewall –adiabatic- ($r = R_0$)

$$\frac{\partial T}{\partial r} = 0;\ \frac{\partial Y_i}{\partial r} = 0;\ \frac{\partial u_x}{\partial r} = 0;\ u_r = 0 \tag{12}$$

(3) and bottom of the pellet –adiabatic- ($x = 0$)

$$\frac{\partial T}{\partial x} = 0;\ \frac{\partial Y_i}{\partial x} = 0;\ u_x = 0;\ \frac{\partial u_r}{\partial x} = 0 \tag{13}$$

(4) For the centre of the cylindrical pellet ($r = 0$)

$$\frac{\partial T}{\partial r} = 0;\ \frac{\partial Y_i}{\partial r} = 0;\ \frac{\partial u_x}{\partial r} = 0;\ \frac{\partial u_r}{\partial r} = 0 \tag{14}$$

3.4. Pyrolysis scheme

When pyrolyzing large biomass particles, both primary and secondary reactions can take place simultaneously, making difficult to determine experimentally their individual contribution to the product yields, which is then often indirectly calculated [9,16]. However, this issue can be solved with the aid of numerical models. This work adopts a kinetic scheme that consists of primary reactions and homogeneous secondary tar reaction. Heterogeneous secondary tar reaction and other related reactions are not considered in this work, but they will in a future model improvement.

3.4.1. Primary reaction kinetics

The pyrolysis kinetic scheme reported by Ranzi et al. [31] is adopted, since it is capable of providing detailed information regarding product composition of gas, tar and char. The primary reaction mechanism considers biomass composed by five components: cellulose (CELL), hemicellulose (HCE), and three varieties of lignin -oxygen-rich lignin (LIGO), carbon-rich lignin (LIGC) and hydrogen-rich lignin (LIGH). Each component decomposes independently through a multistep, branched first-order mechanism, lumped reactions, producing intermediate solid species, char, gases, tars, and adsorbed gases [15]. The rate expressions and stoichiometry of these lumped reactions were validated on the basis of thermo-gravimetric data of small particles, with negligible internal resistances (low heating rate and low temperature). As it is very difficult to experimentally validate kinetic schemes at high temperature due to the increasingly interference of chemical and transport processes, intrinsic kinetic schemes that have been validated for low temperatures are extrapolated to higher temperature conditions ($T > 1200$ °C), acknowledging that it represents an approximation to the real behaviour. The reactions, kinetic parameters and heats of reaction are detailed in Table A.

3.4.2. Intra-particle secondary reactions

When pyrolyzing thermally thick biomass particles, the volatiles residence time inside the pores may be sufficient for tar to react and decompose while circulating towards the particle surface. Moreover, at high heating rates, the produced char layer acts as a catalyst and it provides a lower activation energy path for the tar decomposition [16], resulting in a modification of the product yields: the amount of emitted tars is

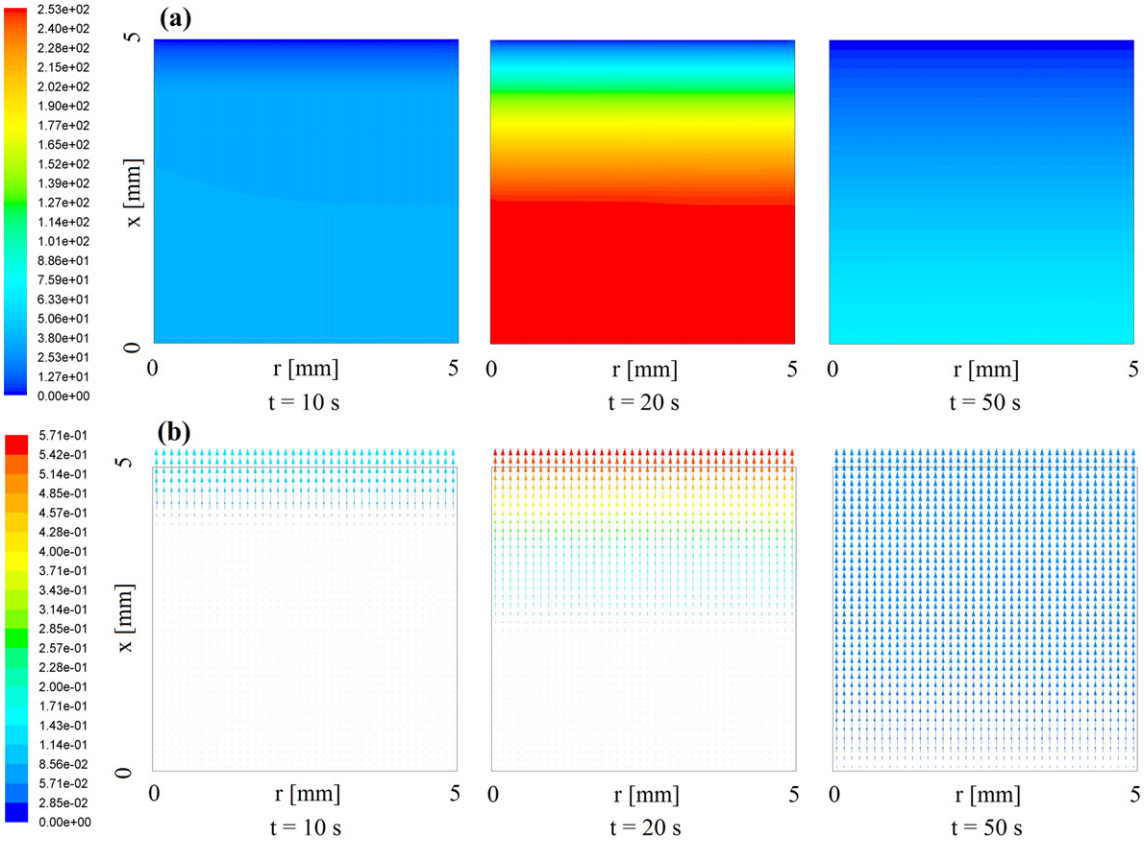

Fig. 3. (a) Instantaneous contour of gauge pressure (Pa) and (b) velocity vectors (m/s) at different times (HR = 50 °C/s and T = 1200 °C).

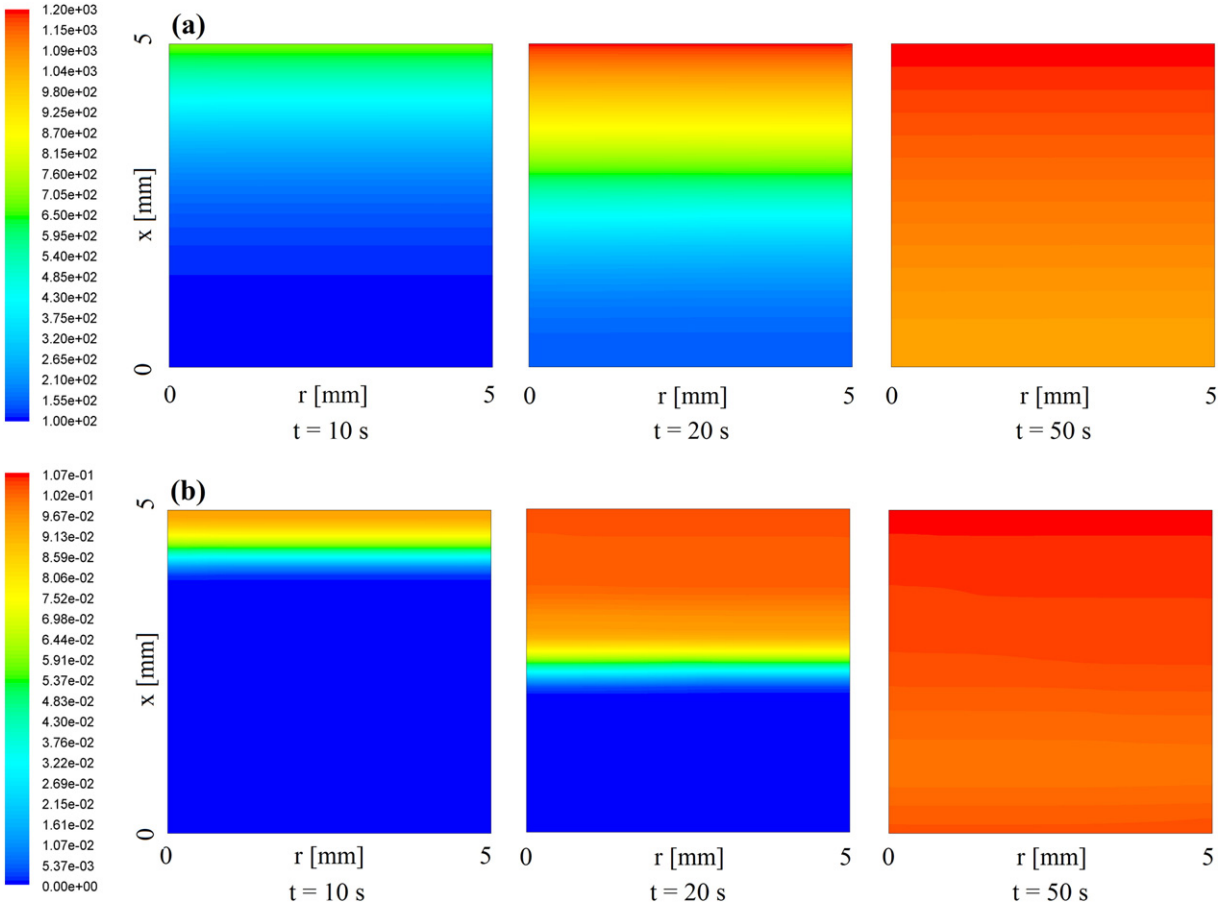

Fig. 4. (a) Instantaneous contour plots of temperature (°C) and (b) char yield layer at different times (HR = 50 °C/s and T = 1200 °C).

reduced while the amount of light gaseous products escaping the particle is increased.

Blondeau and Jeanmart [32] performed an analysis of the scheme proposed by Ranzi et al. [31], and suggested a set of homogeneous secondary tar reactions in order to better predict gas and tar emissions. Then, Mellin et al. [33] adopted the reaction scheme proposed by Blondeau and Jeanmart [32] and included it in a CFD fluidized bed model for pyrolyzing particles of biomass. In this context, following their approach, a modified set of secondary tar reactions was proposed in this work, by means of an elemental balance, taking into account the main light gases measured experimentally, with the stoichiometric coefficients obtained by a thermodynamic calculation (Table B). It is important to mention that these are hypothetical reactions that have not been validated experimentally but are still helpful to explore this aspect [33].

3.5. Material and transport properties

The model considers that all physical parameters depend on the temperature and/or the medium composition. In this context, the evolution of the effective permeability, of the pore diameter and of the effective solid phase thermal conductivity of the solid is obtained by linear interpolation between the property values of the virgin fuel and char (Eq. 15).

$$X = (1-x_B)X_B + x_B X_C, \left(X = K, d_{pore}, k_s\right) \tag{15}$$

$$x_B = \frac{\rho_{B,0}-\rho_B}{\rho_{B0}} \tag{16}$$

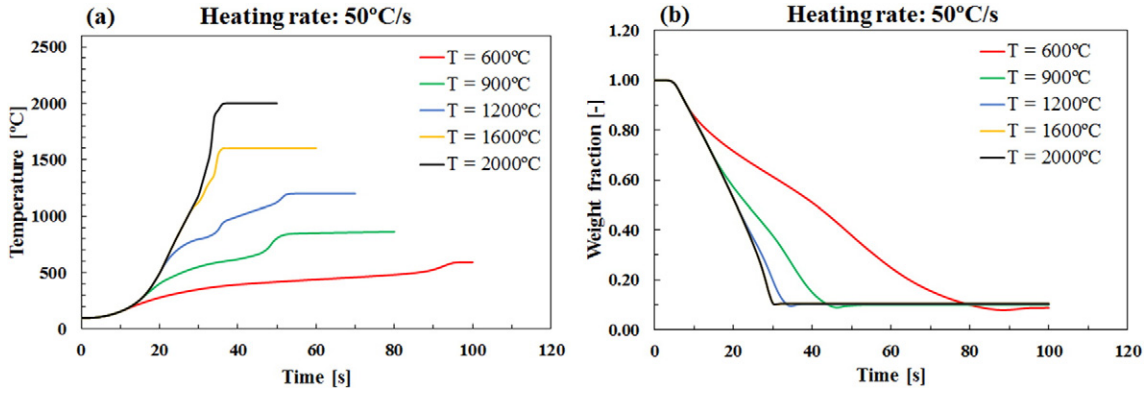

Fig. 5. (a) Temperature profile at the particle centre and (b) weight fraction evolution, for 50 °C/s at different final temperatures.

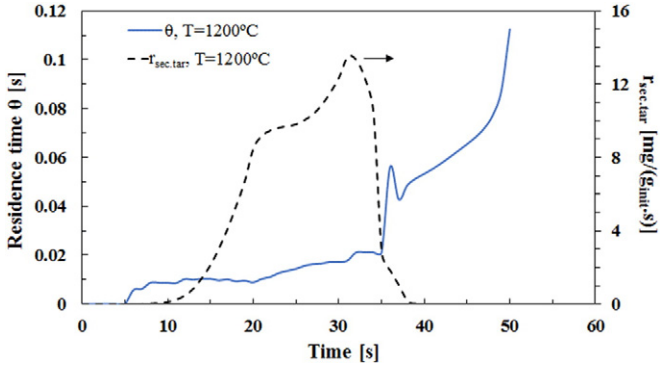

Fig. 6. Intra-particle residence time and secondary tar cracking (dot lines) through the char layer ($T = 1200$ °C, HR = 50 °C/s).

The overall effective thermal conductivity is obtained by averaging the solid and gas phase conductivities.

$$k_{eff} = (1-\varepsilon)k_s + \varepsilon\left(k_g + k_{rad}\right) \tag{17}$$

The radiant contribution is calculated as given by Chan et al. [34].

$$k_{rad} = \frac{13.5\sigma T^3 d_{pore}}{e} \tag{18}$$

The evolution of porosity is given by

$$\varepsilon = 1-\frac{\rho_B}{\hat{\rho}_B}-\frac{\rho_C}{\hat{\rho}_C}. \tag{19}$$

Where $\hat{\rho}_B = \frac{\rho_B}{1-\varepsilon_0}$.

According to the literature, carbon monoxide and levoglucosan are usually the main products in permanent gas and tar, respectively [5,12,35]. Hence, for the sake of simplicity, they were chosen as model compounds for both the permanent gas and tar for calculating molecular diffusivities. Molecular diffusivity is calculated according to Fuller's expression [36]:

$$D_{AB} = \frac{1.10^{-07}T^{1.75}M_{AB}^{0.5}}{P\left[\left(\sum v_A\right)^{1/3}+\left(\sum v_B\right)^{1/3}\right]^2}. \tag{20 – a}$$

Both molecular (Eq. (20-a)) and Knudsen (Eq. (20-b)) diffusions [37] are considered. Bosanquet formula (valid strictly for equimolar counter diffusion) [38] is used to represent the diffusion within the porous region, D_{pore}, (Eq. (20-c)). The effective diffusivity is estimated by including the diffusion coefficient in the pores through the solid porosity, ε, and the tortuosity factor, τ (Eq. (20-d)). Table 3 resumes the values and expressions adopted for the material properties.

$$D_{K,i} = \frac{d_{pore}}{3}\sqrt{\frac{8R}{\pi M_{w,i}}}.T^{1/2} \tag{20 – b}$$

$$D_{pore} = \left(\frac{1}{D_{m,i}}+\frac{1}{D_{K,i}}\right)^{-1} \tag{20 – c}$$

$$D_{eff,i} = \left(\frac{\varepsilon}{\tau}\right)D_{pore} \tag{20 – d}$$

Table 4
Calculated values of maximum tar decomposition rate and amount mass of cracked tar (HR = 50 °C/s).

Temperature [°C]	600	1200	2000
Max. r_{tar} [mg/(g_{init}·s)]	0.21	13.31	30.37
Tar mass cracked [mg/g_{init}]	16.13	191.70	230.77

3.6. Numerical procedure

Initially, the pores were assumed to be filled with argon, with an internal initial velocity set to zero in order to allow argon diffuse towards the surface. As the pyrolysis reactions proceed tar and gas are generated, causing the argon to be expelled out of the pellet domain. In this work, the argon flow rate was much larger than the amount of volatiles released. Therefore, for simplification, it was considered that argon removed the released tar and gas from the solid surface immediately and that the surface was exposed only to argon. Then, the mass concentrations of other gases at the bulk were set to 0.

The governing equations presented in Section 3.2 were solved in 2D–DP using the finite volume discretization method with the CFD software ANSYS FLUENT 14.0. An extensive set of UDFs routines was programmed and added to the code so as to represent the pellet pyrolysis. The "pressure-based method" [41] was used as the algorithm for solving the governing equations. For all scalars, second order discretization scheme was adopted, so as to increase accuracy. Also, in order to avoid possible instabilities in the solution, appropriate under-relaxation factors were set.

Moreover, time step was set to 0.005–0.001 s, and residuals (conversion criteria) were all fixed at 1.10^{-6}. As initial condition, a uniform temperature was assigned to the irradiated top surface, with a value set at 200 °C (in accordance with the experimental measurements). Drying stage is not programmed due to the pellet preparation: the moisture content was removed in an oven before pyrolyzing the pellet. Thus, moisture evaporation was not modelled.

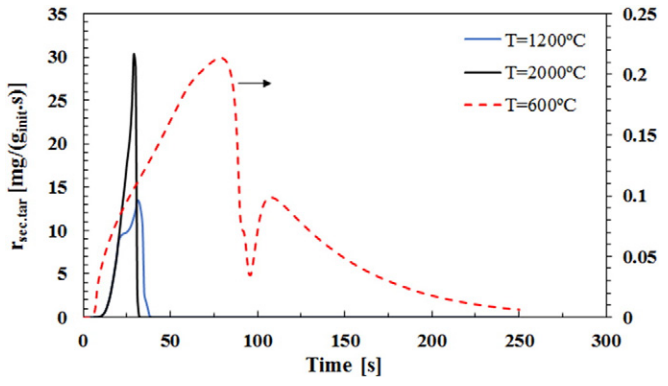

Fig. 7. History of intra-particle tar reaction in time (for 50 °C/s).

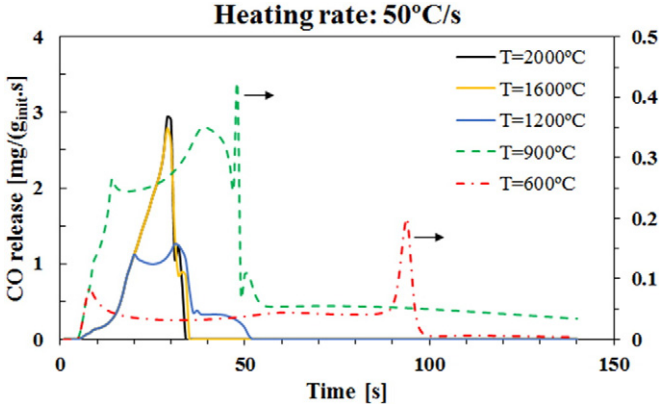

Fig. 8. CO mass flow time history at particle surface (HR = 50 °C/s).

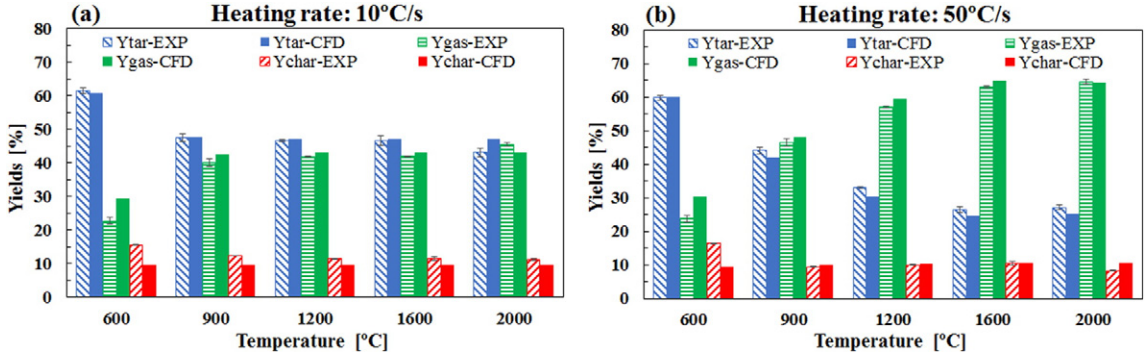

Fig. 9. Model predictions for product yields: (a) gas yield at 10 °C/s, (b) gas yield at 50 °C/s, (c) tar yield at 10 °C/s, (d) tar yield at 50 °C/s, (e) char yield at 10 °C/s and (f) char yield at 50 °C/s.

4. Results and discussion

4.1. Dynamic behaviour of pellet pyrolysis

The validation of the model was achieved by comparing the predicted results against experimental data from solar pyrolysis for five final temperatures (600, 900, 1200, 1600 and 2000 °C) and two heating rates (10 and 50 °C/s). The first part of this section presents information delivered by CFD simulation for a representative case ($T = 1200$ °C and HR = 50 °C/s). A similar analysis can be performed to the other conditions simulated. Finally, experimental and CFD results regarding mass product yields and permanent gas distribution for the whole range of the studied operating conditions are compared and discussed.

4.1.1. Intra-particle pressure and velocity vectors

Contour plots of the intra-particle gauge pressure and velocity vectors of volatile products at different pyrolysis times are given in Fig. 3. The volatile species formation increases the pressure inside the pellet, which is the driving force of velocity. As a result of the pressure gradient, tar and gas move towards the pellet surface. Moreover, a high heating rate produces a rapid formation of volatile products, leading to a sudden increase of internal pressure. Also, as biomass' conversion front progresses, so does the char permeability, allowing tar and gas to exit the particle with fewer restrictions. This behaviour agrees well with the observations reported previously [27,29].

4.1.2. Temperature profile and mass loss history

Fig. 4 shows the temperature and char yield contour plots at 10, 20 and 50 s. It can be seen that during pyrolysis a thermal gradient appears and tends to reduce as pyrolysis time passes. Then, at the end of the process, almost the whole pellet reaches uniform temperature condition. This thermal gradient generates a non-uniform pyrolysis profile, where the bottom of the pellet is the last region to pyrolyze. As a result, the formed tar traverses the char layer with high enough temperature to

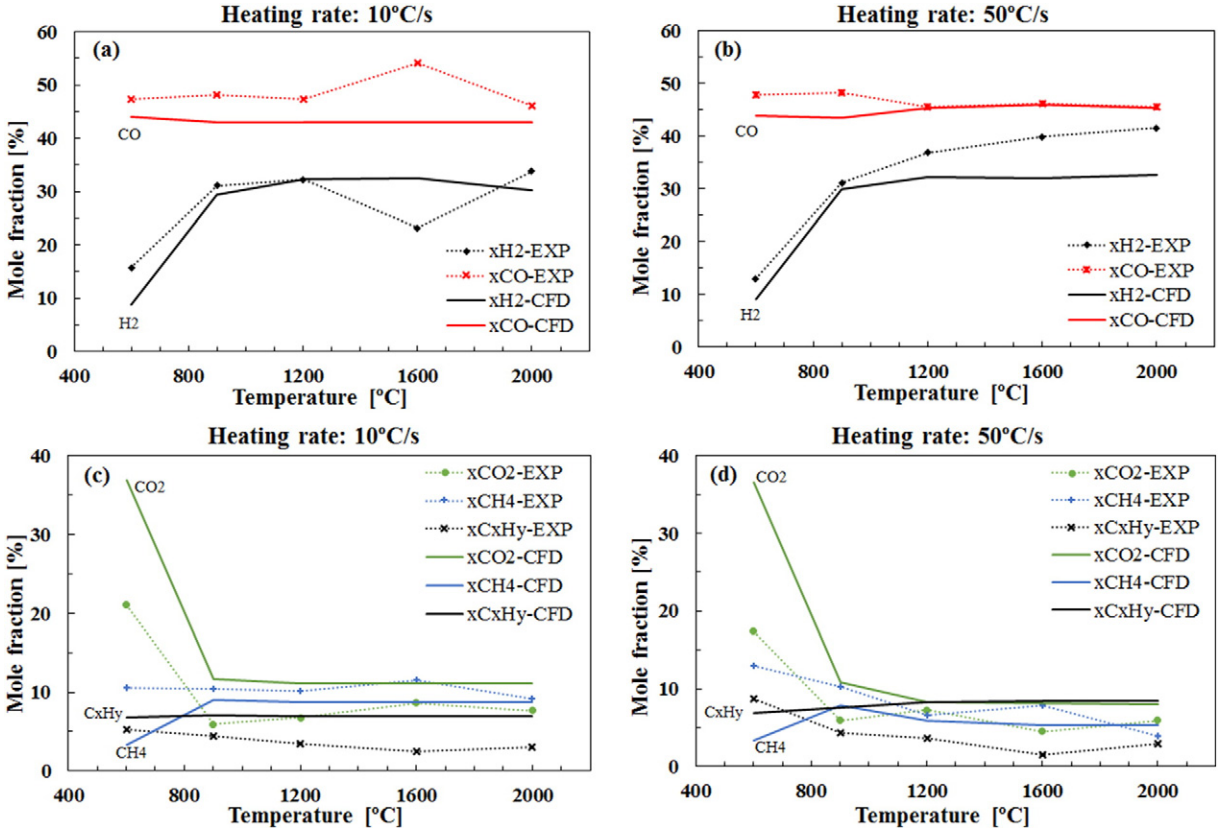

Fig. 10. Comparison of permanent gas species compositions between experimental results and CFD predictions. (a) CO and H_2 at 10 °C/s, (b) CO and H_2 at 50 °C/s, (c) CO_2, CH_4 and C_xH_y at 10 °C/s and CO_2, CH_4 and C_xH_y at 50 °C/s. Experimental dot lines are only a guide-to-the-eye.

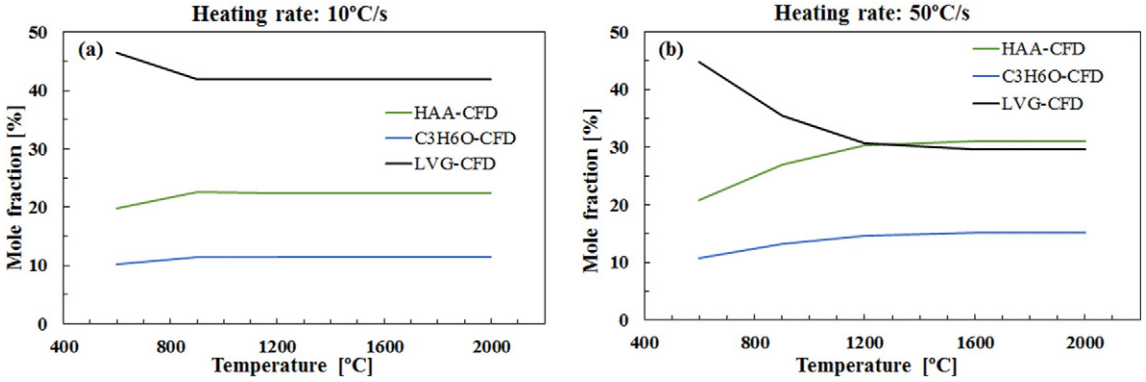

Fig. 11. Mole fractions of the main tar products predicted by the CFD model at (a) 10 °C/s and (b) 50 °C/s.

increase the tar decomposition into permanent gas. Additionally, different heating rate zones also appear inside the particle because of its structural evolution as well as heat transport phenomena. The highest heating rate regions are adjacent to the pellet surface and, as tar forms rapidly and its residence time is short, it leaves the particle without decomposing thus producing more char. Also, different heating rate regions lead to a slight change of char distribution in the particle.

Fig. 5a represents the pellet centre temperature history for the various operating temperatures analysed, at 50 °C/s. The regions where the slope decreases can be caused by endothermic reactions associated to the formation of volatile species and their vaporization [6,25,42]. This qualitative behaviour of the internal temperature profiles of a thick particle is in agreement with several studies found in literature [15,25,26,30].

Fig. 5b displays the weight fraction evolution of the pyrolyzed pellet under various final temperatures (600 to 2000 °C) at 50 °C/s. When analysing the temperature effect, the influence of this operating condition is negligible at the process onset where all the curves overlap, as reported by Okekunle et al. [29]. Then as final temperature increases, so does the heat transfer rate, thereby accelerating the pyrolysis reactions. Consequently, the weight loss rate increases with temperature.

It can be seen that at the end of pyrolysis, the weight fraction reaches a minimum and then slightly increases to the final value. This behaviour can be explained by the tar cracking reactions. The last fraction of produced tar occurs at the bottom of the pellet. Hence, tar must pass through the whole pellet at temperature near to that of the final operating conditions and with a relative low velocity (as explained previously), which results in a longer residence time. Consequently, tar species decompose leading to a small increase in char production. Also, as temperature increases, the mass loss weight curves tend to get proximate, which is consistent with a transition from mixed control (kinetic and heat transfer) to pure heat transfer control of the pyrolysis rate.

4.1.3. Volatiles residence time and intra-particle secondary tar reaction

The intra-particle residence time θ can be defined as:

$$\theta(t) = \frac{L_{char}(t)}{\overline{v}_g|_{char\ layer}(t)} \qquad (20-c)$$

where L_{char} is the char layer length at a given time, and $\overline{v}_g$ represents the volatiles average velocity in this region. Thus, the residence time varies as the char front progresses towards the bottom of the pellet. Fig. 6 displays θ values through the pyrolysis process at $T = 1200$ °C and HR = 50 °C/s. Two regions of different θ can be distinguished. For $t < 20$ s, a region of low values of θ ($\overline{\theta} \approx 0.01\ s$) can be attributed to the high values of tar formation rate (and intra-particle pressure that causes tar to be expelled rapidly) located at the upper region of the pellet. Then, for $t > 20$ s, the intra-particle pressure gradient is reduced (as well as the flow rate) and the char layer increases, resulting in a considerable increase of the volatiles residence time ($\overline{\theta} \approx 0.02\ s$).

The tar cracking reaction is the result of two factors, the intra-particle residence time and the temperature level at the char layer. For $t < 20$ s, although the residence time is relatively short, tar cracking is enhanced due to the higher temperature values near the pellet surface. For $t > 20$ s, the combined effect of an increase in residence time and temperature of the char layer leads tar decomposition rate to a maximum. After 40 s, the secondary tar decomposition is finished and the resulting residence time is related to the permanent gas species.

Fig. 7 displays tar consumption rate at three different final temperatures: 600, 1200 and 2000 °C at 50 °C/s. At 600 °C, secondary pyrolysis rate is almost negligible. Then, as temperature increases, so does the reaction rate and the maximum rate value is achieved faster, as expected. An integration of the reaction rate gives the amount of tar mass decomposed into permanent gas and char. Table 4 presents the maximum values of r_{tar} as well as the cracked mass. It can be appreciated that for $T > 1200$ °C, intra-particle secondary reactions play a significant role on the product yields, despite the decrease in tar intra-particle residence time.

Fig. 8 plots the influence of final temperature on CO release mass flow rate for HR = 50 °C/s. It can be observed that an increase in final temperature modifies the maximum values of CO release. The significant increase in the CO release rate with time results from the intra-particle tar secondary reactions that are enhanced at higher temperatures.

For T≤1200 °C, two distinctive peaks can be observed. The first peak could be produced by the primary pyrolysis, while the second peak could be the result of tar intra-particle decomposition. However, for T>1200 °C the second peak tends to overlap with the first one, indicating that both primary and secondary pyrolyses may occur almost simultaneously.

4.1.4. Char, tar and gas yield

4.1.4.1. Influence of final temperature. Figs. 9a-f present the predicted yields of gas, liquid (tar) and char at different temperatures and heating rates considered in this work, and compare them against the experimental measurements and the results from Zeng et al. Model [29]. As shown in Fig. 9, both approaches predict well the experimental gas, tar and char yields for the studied operating conditions, where the trend suggests that the higher the temperature, the higher the gas yield. The main discrepancy takes place for the lowest final temperature case (600 °C), where the present model underestimates the char yield (Zeng et al. model fits better the experimental char yield), whereas for all higher temperatures there is a very good agreement between the experimental data of tar and gas yields and the predicted values obtained by the model.

For the two heating rates analysed, the experimental char yield diminishes in the temperature range 600–900 °C. Then, for $T > 900$ °C, both the experimental and predicted results indicate that the char yield remains almost constant. At 10 °C/s heating rate, CFD results indicate that the temperature influence on the gas and tar yields is significant between 600 °C and 900 °C, then for temperatures above 900 °C its influence is almost negligible, which is in accordance with the experimental measurements. Only at $T = 2000$ °C, it was observed that the experimental gas yield was slightly higher than the tar yield. On the other hand, for a heating rate of 50 °C/s, the temperature has a significant influence on the tar and gas yields up to 1600 °C. Homogeneous reactions are not significant at the lowest temperature studied, but higher final temperature favours the tar secondary reactions in the biomass pellet [43]. Consequently, a large fraction of tar components decomposes, and the gas fraction increases significantly, as pointed out by numerous researches [44–46]. This behaviour is very well reproduced by the model.

4.1.4.2. Influence of heating rate. It can be seen that an increase in the HR produces a significant modification in the product yields of tar and gas. At 10 °C/s the tar yield is always higher than the gas yield. However, for the highest heating rate (50 °C/s) and for final temperatures above 900 °C, the gas yield becomes higher than the tar yield.

Liquid yields predicted by the model fit excellently to the experimental measurements for the two HR analysed, as shown in Fig. 9. Results indicate that the higher the HR, the lower the tar yield. When analysing liquid yield production as the heating rate increases, two opposite effects can be distinguished: (1) a considerable amount of tar may leave the pellet without decomposing due to a diminution in the tar intra-particle residence time; (2) a fast increase of the tar temperature quickly decomposes the liquid fraction into gas and char. For the pellet size used in this study, results may indicate that the second effect may be more significant than the first one, improving the intra-particle tar decomposition.

4.1.5. Gas composition

4.1.5.1. Influence of final temperature. Fig. 10a-d shows a detailed comparison of experimental and predicted major light gases yields. Trends are generally well predicted, and the model estimations are quantitatively in reasonably good agreement with experimental data. With an increase in temperature, secondary tar cracking (mostly from the degradation of cellulose at high temperature) produces mainly CO and H_2 [47].

CO is in both cases the most abundant gaseous product, accounting for a mole fraction higher than 40% and practically no variation as temperature increases. For the case of H_2, the mole fraction increases rapidly with temperature until 1200 °C, and then remains almost constant for higher temperatures. A sudden increase is observed in the experimental mole fraction for CO at $T = 1600$ °C, which can be inferred to experimental uncertainty. Indeed, for the highest temperature case the CO composition decreases again to a value similar to those obtained for the temperature range 600–1200 °C. The same consideration can be applied to H_2.

The most significant difference between the CFD predictions and the experimental data for CO_2 at both heating rates, occurs at the lowest studied temperature (600 °C), which indicates that the primary reaction stoichiometry may overestimate the CO_2 production, since the actual model does not consider the CO_2 formation by homogeneous secondary tar reactions.

4.1.5.2. Influence of heating rate. From Fig. 10a and b, it can be observed experimentally that the higher the HR, the higher the H_2 composition in the gaseous products. This influence is well predicted by the model for heating rate of 10 °C/s. Additionally, at 50 °C/s, the model is in good agreement for temperatures below 1200 °C. Then the model shows that the H_2 mole fraction remains almost constant when the temperature increases. On the contrary, both the model results and the experimental data indicate that an increase in the heating rate does not have a considerable influence on the CO production.Finally, the CFD model reports that the influence of HR on product distribution of CO_2, CH_4 and C_xH_y is less significant, in agreement with experimental measurements.

4.1.6. Tar composition

Even if experimental measurements concerning tar speciation were not carried out, the mole fraction of the main three tar compounds predicted by the model are presented in Fig. 11a-b. At a heating rate of 10 °C/s, Levoglucosan accounts for the highest mole fraction in tar (>41%) for the whole temperature range. However, at a heating rate of 50 °C/s, the model indicates that LVG mole fraction decreases as temperature increases. For $T > 1600$ °C, HAA becomes the most abundant compound in tar. Then, a further increase in temperature has a negligible impact on tar product distribution.

5. Conclusions

A 2D unsteady model for representing the behaviour of a single cylindrical biomass pellet under radiatively-induced fast pyrolysis was formulated in the frame of CFD tool ANSYS-FLUENT and validated against experimental data obtained in a solar facility. A detailed primary pyrolysis kinetic scheme, intra-particle transport phenomena as well as intra-particle tar decomposition and structural characteristics were included by a set of self-developed UDFs. This new approach improves a simpler single particle model developed previously [30]. The primary pyrolysis reactions scheme was adopted from the multi-component mechanism proposed by Ranzi et al. [31], whereas a secondary intra-particle homogeneous tar reactions scheme was proposed based on thermodynamic calculations. Consequently, the model is capable of predicting the pyrolysis behaviour for a wide range of feedstocks and operating conditions. Additionally, the model enables predicting not only char, tar and gas yields, but also the species composition of the two latter products (gas and tar).

The simulation results were compared to experimental data at two heating rates (10 °C/s and 50 °C/s) and five final temperatures (600, 900, 1200, 1600 and 2000 °C). This comparison showed a good agreement with the measured data. CFD results indicate that moving towards the particle centre, the heating rate decreases resulting in a non-uniform char profile inside the particle. Both the experimental and simulation results showed that an increase in the HR enhances intra-particle tar decomposition, thus decreasing tar yield and producing more gas. Additionally, the influence of HR on H_2 distribution is significant as temperature increases, unlike CO where the heating rate influence is negligible for the temperature range analysed.

Although the kinetics adopted in this work are suitable for low and moderate HR and temperature levels, they can be applied for the case of fast pyrolysis of thermally thick particles with a good accuracy. Future work for improving the proposed model will concern the inclusion of heterogeneous chemical reactions to the kinetic scheme. Finally, the model can be adapted and included in any process simulation where pyrolysis occurs even under high HR and temperature levels, and it can be possibly coupled to a reactor scale model.

Acknowledgements

This work was developed in the frame of the SYNSOLGAS CAFCI Project (CONICET-MINCyT-CNRS), an Argentine-French collaboration and was supported by French "Investments for the future" programme managed by the National Agency for Research under contract ANR-10-LABX-22-01, labex SOLSTICE. J. Soria and G. Mazza are Research Members of CONICET (Argentine).

Table A
Biomass primary pyrolysis kinetic mechanism, kinetic parameters and heats of reaction [31].

	Reaction			A [s^{-1}]	Ea [J/kmol]	ΔH^0_R [J/kg]
1	CELL	→	CELLA	4.00×10^{13}	1.884×10^{8}	0
2	CELLA	→	0.8HAA + 0.2GLYOX + 0.1C_2H_4O + 0.25HMFU + 0.3C_3H_6O + 0.21CO_2 + 0.1H_2 + 0.4CH_2O + 0.16CO + 0.1CH_4 + 0.83H_2O + 0.02HCOOH + 0.61Char	5.00×10^{8}	1.214×10^{8}	6.200×10^{5}
3	CELLA	→	LVG	1.8 T	4.190×10^{7}	3.640×10^{5}
4	CELL	→	5H_2O + 6Char	4.00×10^{7}	1.298×10^{8}	-1.913×10^{6}
5	HCE	→	0.4HCE1 + 0.6HCE2	3.3×10^{9}	1.298×10^{8}	1.000×10^{5}
6	HCE1	→	0.025H_2O + 0.5CO_2 + 0.025HCOOH + 0.5CO + 0.8CH_2O + 0.125C_2H_5OH + 0.1CH_3OH + 0.25C_2H_4 + 0.125G{H_2} + 0.275G{CO_2} + 0.4G{CH_2O} + 0.45G{CH_3OH} + 0.325G{CH_4} + 0.875Char	1.00×10^{9}	1.340×10^{8}	-9.200×10^{4}
7	HCE1	→	0.25H_2O + 0.5CO_2 + 0.05HCOOH + 0.3CO + 0.15G{CO} + 0.25G{CO_2} + 1.7G{CH_2O} + 0.625G{CH_4} + 0.375G{C_2H_4} + 0.675 Char	0.05*T	3.350×10^{7}	-1.860×10^{6}
8	HCE1	→	XYLAN	0.9*T	4.605×10^{7}	5.880×10^{5}
9	HCE2	→	0.2H_2O + 0.175CO + 0.275CO_2 + 0.5CH_2O + 0.1C_2H_5OH + 0.2HAA + 0.025HCOOH + 0.25G{CH4} + 0.3G{CH_3OH} + 0.275G{C_2H_4} + 0.4G{CO_2} + 0.925G{CH_2O} + Char	3.30×10^{9}	1.382×10^{8}	2.120×10^{5}
10	LIGC	→	0.35LIGCC + 0.1COUMARYL + 0.08PHENOL + 0.41C_2H_4 + H_2O + 0.3CH_2O + 0.32CO + 0.7G{CH_2O} + 0.495 G{CH_4} + 5.735Char	1.33×10^{5}	2.030×10^{8}	-4.900×10^{5}
11	LIGH	→	LIGOH + C_3H_6O	6.70×10^{12}	1.570×10^{8}	1.000×10^{5}
12	LIGO	→	LIGOH + G{CO_2}	3.30×10^{8}	1.068×10^{8}	4.460×10^{5}
13	LIGCC	→	0.3COUMARYL + 0.2PHENOL + 0.35HAA + 0.7H_2O + 0.4CO + 0.65G{CH_4} + 0.6G{C_2H_4} + G{CH_2O} + 0.4G{CO} + 6.75Char	1.60×10^{6}	1.319×10^{8}	-5.030×10^{5}
14	LIGOH	→	LIG + 0.15G{H_2} + 0.9H_2O + 0.1CH_4 + 0.5CH_3OH + 0.5G{CH_3OH} + 0.05CO_2 + 0.3CO + G{CO} + 0.05HCOOH + 0.6G{CH_2O} + 0.35G{CH_4} + 0.2G{C_2H_4} + 4.15Char	5.00×10^{7}	1.256×10^{8}	-1.200×10^{5}
15	LIGOH	→	1.5H_2O + 0.5CO + 0.1CH_4 + 0.5G{H_2} + 1.6G{CO} + 3.9G{CH_2O} + 1.65G{CH_4} + 0.3G{C_2H_4} + 0.5G{CH_3OH} + 10.15Char	33	6.280×10^{7}	-1.604×10^{6}
16	LIG	→	FE2MACR	2.4*T	5.024×10^{7}	6.860×10^{5}
17	LIG	→	0.95H_2O + 0.2CH_2O + 0.4CH_3OH + CO + 0.2CH_4 + 0.05HCOOH + 0.45G{CO} + 0.5G{CH2O} + 0.4G{CH_4} + 0.65G{C_2H_4} + 0.2C_2H_4O + 0.2C_3H_6O + 5.5Char	4.00×10^{8}	1.256×10^{8}	-4.700×10^{5}
18	LIG	→	0.6H_2O + 0.4CO + 0.2CH_4 + 0.4CH_2O + 0.2G{CO} + 0.4G{CH_4} + 0.5G{C_2H_4} + 0.4G{CH_3OH} + 2G{COH_2} + 6Char	0.083*T	3.350×10^{7}	-1.663×10^{6}
19	G{CO_2}	→	CO_2	1.00×10^{6}	1.005×10^{8}	-1.814×10^{6}
20	G{CO}	→	CO	5.00×10^{12}	2.093×10^{8}	-2.000×10^{6}
21	G{CH_2O}	→	CO + H_2	5.00×10^{11}	2.973×10^{8}	6.778×10^{6}
22	G{H_2}	→	H_2	5.00×10^{11}	3.140×10^{8}	0
23	G{CH_4}	→	CH_4	5.00×10^{12}	3.002×10^{8}	0
24	G{C_2H_4}	→	C_2H_4	5.00×10^{12}	3.002×10^{8}	0
25	G{CH_3OH}	→	CH_3OH	2.00×10^{12}	2.093×10^{8}	0

Table B
Proposed tar cracking reaction kinetic mechanism. Kinetic parameters (A and Ea) were taken from [22].

Reaction			A[s^{-1}]	Ea [J/kmol]	ΔH^0_R [J/kg]
HAA	→	$2CO + 2H_2$	4.28×10^6	1.08×10^8	3.563×10^6
GLYOX	→	$2CO + H_2$	4.28×10^6	1.08×10^8	-1.566×10^5
C_3H_6O	→	$CO + H_2 + C_2H_4$	4.28×10^6	1.08×10^8	1.878×10^6
HMFU	→	$3CO + 1.5C_2H_4$	4.28×10^6	1.08×10^8	6.427×10^5
LVG	→	$5CO + 4H_2 + 0.5C_2H_4$	4.28×10^6	1.08×10^8	1.702×10^6
XYL	→	$4CO + 3H_2 + 0.5C_2H_4$	4.28×10^6	1.08×10^8	-5.630×10^5
pCOUMARYL	→	$2CO + 2.5C_2H_4 + 2Char$	4.28×10^6	1.08×10^8	-3.596×10^5
PHENOL	→	$CO + 1.5C_2H_4 + 2Char$	4.28×10^6	1.08×10^8	-1.431×10^5
FE2MACR	→	$4CO + 3C_2H_4 + Char$	4.28×10^6	1.08×10^8	-6.938×10^5

References

[1] A.V.V. Bridgwater, Review of fast pyrolysis of biomass and product upgrading, Biomass Bioenergy 38 (2012) 68–94, http://dx.doi.org/10.1016/j.biombioe.2011.01.048.
[2] T. Kan, V. Strezov, T.J. Evans, Lignocellulosic biomass pyrolysis: a review of product properties and effects of pyrolysis parameters, Renew. Sust. Energ. Rev. 57 (2016) 126–1140, http://dx.doi.org/10.1016/j.rser.2015.12.185.
[3] D. Baruah, D.C. Baruah, Modeling of biomass gasification: a review, Renew. Sust. Energ. Rev. 39 (2014) 806–815, http://dx.doi.org/10.1016/j.rser.2014.07.129.
[4] A. Demirbas, G. Arin, An overview of biomass pyrolysis, Energy Sources 24 (2002) 471–482.
[5] M.S. Mettler, G. Vlachos, P.J. Dauenhauer, Environmental science top ten fundamental challenges of biomass pyrolysis for biofuels, Energy Environ. Sci. 7 (2012) 7797–7809, http://dx.doi.org/10.1039/c2ee21679e.
[6] M. Van de Velden, J. Baeyens, A. Brems, B. Janssens, R. Dewil, Fundamentals, kinetics and endothermicity of the biomass pyrolysis reaction, Renew. Energy 35 (2010) 232–242, http://dx.doi.org/10.1016/j.renene.2009.04.019.
[7] M. Jahirul, M. Rasul, A. Chowdhury, N. Ashwath, Biofuels production through biomass pyrolysis —a technological review, Energies 5 (2012) 4952–5001, http://dx.doi.org/10.3390/en5124952.
[8] A.V. Bridgwater, D. Meier, D. Radlein, An overview of fast pyrolysis of biomass, Org. Geochem. 30 (1999) 1479–1493, http://dx.doi.org/10.1016/S0146-6380(99)00120-5.
[9] C. Di Blasi, Modeling chemical and physical processes of wood and biomass pyrolysis, Prog. Energy Combust. Sci. 34 (2008) 47–90, http://dx.doi.org/10.1016/j.pecs.2006.12.001.
[10] R. Li, K. Zeng, J. Soria, G. Mazza, D. Gauthier, R. Rodriguez, G. Flamant, Product distribution from solar pyrolysis of agricultural and forestry biomass residues, Renew. Energy 89 (2016) 27–35, http://dx.doi.org/10.1016/j.renene.2015.11.071.
[11] A. Nzihou, G. Flamant, B. Stanmore, Synthetic fuels from biomass using concentrated solar energy – a review, Energy 42 (2012) 121–131, http://dx.doi.org/10.1016/j.energy.2012.03.077.
[12] M.N. Uddin, W.M.A. Wan Daud, H.F. Abbas, Effects of pyrolysis parameters on hydrogen formations from biomass: a review, RSC Adv. 4 (2014) 10467–10490, http://dx.doi.org/10.1039/c3ra43972k.
[13] K. Zeng, D. Gauthier, R. Li, G. Flamant, Solar pyrolysis of beech wood: effects of pyrolysis parameters on the product distribution and gas product composition, Energy 93 (2015) 1648–1657, http://dx.doi.org/10.1016/j.energy.2015.10.008.
[14] F. Abnisa, W.M.A. Wan Daud, A review on co-pyrolysis of biomass: an optional technique to obtain a high-grade pyrolysis oil, Energy Convers. Manag. 87 (2014) 71–85, http://dx.doi.org/10.1016/j.enconman.2014.07.007.
[15] M. Corbetta, A. Frassoldati, H. Bennadji, K. Smith, M.J. Serapiglia, G. Gauthier, T. Melkior, E. Ranzi, E.M. Fisher, Pyrolysis of centimeter-scale woody biomass particles: kinetic modeling and experimental validation, Energy Fuel 28 (2014) 3884–3898, http://dx.doi.org/10.1021/ef500525v.
[16] T. Pattanotai, H. Watanabe, K. Okazaki, Experimental investigation of intraparticle secondary reactions of tar during wood pyrolysis, Fuel 104 (2013) 468–475, http://dx.doi.org/10.1016/j.fuel.2012.08.047.
[17] C. Di Blasi, Modeling intra- and extra-particle processes of wood fast pyrolysis, AICHE J. 48 (2002) 2386–2397.
[18] G.D. Mazza, J.M. Soria, D. Gauthier, A. Reyes Urrutia, M. Zambon, G. Flamant, Environmental friendly fluidized bed combustion of solid fuels: a review about local scale modeling of char heterogeneous combustion, Waste Biomass Valoriz. 7 (2016) 237–266, http://dx.doi.org/10.1007/s12649-015-9461-5.
[19] K. Kwiatkowski, B. Górecki, J. Korotko, W. Gryglas, M. Dudyński, K. Bajer, Numerical modeling of biomass pyrolysis—heat and mass transport models, Numer. Heat Transf. Part A Appl. 64 (2013) 216–234, http://dx.doi.org/10.1080/10407782.2013.779166.
[20] G. Gentile, A. Cuoci, A. Frassoldati, T. Faravelli, A comprehensive CFD model for the biomass pyrolysis, Chem. Eng. Trans. 43 (2015) 1–6.
[21] C. Di Blasi, Heat, momentum and mass transport through a shrinking biomass particle exposed to thermal radiation, Chem. Eng. Sci. 51 (1996) 1121–1132, http://dx.doi.org/10.1016/S0009-2509(96)80011-X.
[22] R.S. Miller, J. Bellan, A generalized biomass pyrolysis model based on superimposed cellulose, hemicellulose and liqnin kinetics, Combust. Sci. Technol. 126 (1997) 97–137, http://dx.doi.org/10.1080/00102209708935670.
[23] M.G. Gronli, M.C. Melaaen, M. Grønli, M.C. Melaaen, Mathematical model for wood pyrolysis - comparison of experimental measurements with model predictions, Energy Fuel 14 (2000) 791–800, http://dx.doi.org/10.1021/ef990176q.
[24] M. Bellais, Modelling of the Pyrolysis of Large Wood Particles, pH.D Thesis KTH - Royal Institute of Technology, 2007.
[25] W.C. Park, A. Atreya, H.R. Baum, Experimental and theoretical investigation of heat and mass transfer processes during wood pyrolysis, Combust. Flame 157 (2010) 481–494, http://dx.doi.org/10.1016/j.combustflame.2009.10.006.
[26] V. Pozzobon, S. Salvador, J.J. Bézian, M. El-Hafi, Y. Le Maoult, G. Flamant, Radiative pyrolysis of wet wood under intermediate heat flux: experiments and modelling, Fuel Process. Technol. 128 (2014) 319–330, http://dx.doi.org/10.1016/j.fuproc.2014.07.007.
[27] X. Shi, F. Ronsse, J.G. Pieters, Finite element modeling of intraparticle heterogeneous tar conversion during pyrolysis of woody biomass particles, Fuel Process. Technol. 148 (2016) 302–316, http://dx.doi.org/10.1016/j.fuproc.2016.03.010.
[28] A. Anca-Couce, I. Obernberger, Application of a detailed biomass pyrolysis kinetic scheme to hardwood and softwood torrefaction, Fuel 167 (2016) 158–167, http://dx.doi.org/10.1016/j.fuel.2015.11.062.
[29] P.O. Okekunle, T. Pattanotai, H. Watanabe, K. Okazaki, Numerical and experimental investigation of intra-particle heat transfer and tar decomposition during pyrolysis of wood biomass, J. Therm. Sci. Technol. 6 (2011) 360–375, http://dx.doi.org/10.1299/jtst.6.360.
[30] K. Zeng, J. Soria, D. Gauthier, G. Mazza, G. Flamant, Modeling of beech wood pellet pyrolysis under concentrated solar radiation, Renew. Energy 99 (2016) 721–729, http://dx.doi.org/10.1016/j.renene.2016.07.051.
[31] E. Ranzi, M. Corbetta, F. Manenti, S. Pierucci, Kinetic modeling of the thermal degradation and combustion of biomass, Chem. Eng. Sci. 110 (2014) 2–12, http://dx.doi.org/10.1016/j.ces.2013.08.014.
[32] J. Blondeau, H. Jeanmart, Biomass pyrolysis at high temperatures: prediction of gaseous species yields from an anisotropic particle, Biomass Bioenergy 41 (2012) 107–121, http://dx.doi.org/10.1016/j.biombioe.2012.02.016.
[33] P. Mellin, E. Kantarelis, W. Yang, Computational fluid dynamics modeling of biomass fast pyrolysis in a fluidized bed reactor, using a comprehensive chemistry scheme, Fuel 117 (2014) 704–715, http://dx.doi.org/10.1016/j.fuel.2013.09.009.
[34] W.-C.R. Chan, M. Kelbon, B.B. Krieger, Modelling and experimental verification of physical and chemical processes during pyrolysis of a large biomass particle, Fuel 64 (1985) 1505–1513, http://dx.doi.org/10.1016/0016-2361(85)90364-3.
[35] E.M. Suuberg, I. Milosavljevic, V. Oja, Two-regime global kinetics of cellulose pyrolysis: the role of tar evaporation, XXVI Symp. Combust. Combust. 26 (1996) 1515–1521, http://dx.doi.org/10.1016/S0082-0784(96)80373-0.
[36] R.H. Perry, J.O. Maloney, D.W. Green, Perry's Chemical Engineers' Handbook, McGraw-Hill, 1997.
[37] R. Krishna, J.M. van Baten, Investigating the validity of the Bosanquet formula for estimation of diffusivities in mesopores, Chem. Eng. Sci. 69 (2012) 684–688, http://dx.doi.org/10.1016/j.ces.2011.11.026.
[38] G.F. Froment, K.B. Bischoff, Chemical Reactor Analysis and Design, second ed. John Wiley & Sons, 1990.
[39] C. Di Blasi, Modeling intra- and extra-particle processes of wood fast pyrolysis, AICHE J. 48 (2002) 2386–2397, http://dx.doi.org/10.1002/aic.690481028.
[40] H. Thunman, B. Leckner, F. Niklasson, F. Johnsson, Combustion of wood particles - a particle model for Eulerian calculations, Combust. Flame 129 (2002) 30–46, http://dx.doi.org/10.1016/S0010-2180(01)00371-6.
[41] ANSYS Inc, ANSYS FLUENT Theory Guide, ANSYS, Inc., 2011.
[42] C. Di Blasi, C. Branca, F. Masotta, E. De Biase, Experimental analysis of reaction heat effects during beech wood pyrolysis, Energy Fuel 27 (2013) 2665–2674, http://dx.doi.org/10.1021/ef4001709.
[43] O. Onay, Influence of pyrolysis temperature and heating rate on the production of bio-oil and char from safflower seed by pyrolysis, using a well-swept fixed-bed reactor, Fuel Process. Technol. 88 (2007) 523–531, http://dx.doi.org/10.1016/j.fuproc.2007.01.001.
[44] P.A. Horne, P.T. Williams, Influence of temperature on the products from the flash pyrolysis of biomass, Fuel 75 (1996) 1051–1059, http://dx.doi.org/10.1016/0016-2361(96)00081-6.
[45] A. De mirbas, Effects of temperature and particle size on bio-char yield from pyrolysis of agricultural residues, J. Anal. Appl. Pyrolysis 72 (2004) 243–248, http://dx.doi.org/10.1016/j.jaap.2004.07.003.
[46] M. Garcia-Perez, X.S. Wang, J. Shen, M.J. Rhodes, F. Tian, W.J. Lee, H. Wu, C.Z. Li, Fast pyrolysis of oil mallee woody biomass: effect of temperature on the yield and quality of pyrolysis products, Ind. Eng. Chem. Res. 47 (2008) 1846–1854, http://dx.doi.org/10.1021/ie071497p.
[47] J. Rath, G. Staudinger, Cracking reactions of tar from pyrolysis of spruce wood, Fuel 80 (2001) 1379–1389, http://dx.doi.org/10.1016/S0016-2361(01)00016-3.